



## Faculty Publications

---

2017-07-14

# Custom 3D printer and resin for 18 $\mu\text{m}$ $\times$ 20 $\mu\text{m}$ microfluidic flow channels

Hua Gong

Brigham Young University, gonghuabupt@gmail.com

Bryce P. Bickham

Brigham Young University, brycebickham@gmail.com

Adam T. Woolley

Brigham Young University, awoolley@chem.byu.edu

Gregory P. Nordin

Brigham Young University - Provo, nordin@byu.edu

Follow this and additional works at: <https://scholarsarchive.byu.edu/facpub>



Part of the [Computer Engineering Commons](#)

## Original Publication Citation

H. Gong, B. Bickham, A. T. Woolley and G. P. Nordin, Lab Chip, 2017, DOI: 10.1039/C7LC00644F

---

## BYU ScholarsArchive Citation

Gong, Hua; Bickham, Bryce P.; Woolley, Adam T.; and Nordin, Gregory P., "Custom 3D printer and resin for 18  $\mu\text{m}$   $\times$  20  $\mu\text{m}$  microfluidic flow channels" (2017). *Faculty Publications*. 1923.

<https://scholarsarchive.byu.edu/facpub/1923>

This Peer-Reviewed Article is brought to you for free and open access by BYU ScholarsArchive. It has been accepted for inclusion in Faculty Publications by an authorized administrator of BYU ScholarsArchive. For more information, please contact [ellen\\_amatangelo@byu.edu](mailto:ellen_amatangelo@byu.edu).

Cite this: DOI: 10.1039/xxxxxxxxxx

## Custom 3D printer and resin for $18\ \mu\text{m} \times 20\ \mu\text{m}$ microfluidic flow channels<sup>†</sup>

Hua Gong,<sup>a</sup> Bryce P. Bickham,<sup>a</sup> Adam T. Woolley,<sup>b</sup> and Gregory P. Nordin<sup>\*a</sup>

Received Date  
Accepted Date

DOI: 10.1039/xxxxxxxxxx

www.rsc.org/journalname

While there is great interest in 3D printing for microfluidic device fabrication, to-date the achieved feature sizes have not been in the truly microfluidic regime ( $<100\ \mu\text{m}$ ). In this paper we demonstrate that a custom Digital Light Processor stereolithographic (DLP-SLA) 3D printer and a specifically-designed, low cost, custom resin can readily achieve flow channel cross sections as small as  $18\ \mu\text{m} \times 20\ \mu\text{m}$ . Our 3D printer has a projected image plane resolution of  $7.6\ \mu\text{m}$  and uses a 385 nm LED, which dramatically increases the available selection of UV absorbers for resin formulation compared to 3D printers with 405 nm LEDs. Beginning with 20 candidate absorbers, we demonstrate the evaluation criteria and process flow required to develop a high-resolution resin. In doing so, we introduce a new mathematical model for characterizing the resin optical penetration depth based only on measurement of the absorber's molar absorptivity. Our final resin formulation uses 2-nitrophenyl phenyl sulfide (NPS) as the UV absorber. We also develop a novel channel narrowing technique that, together with the new resin and 3D printer resolution, enables small flow channel fabrication. We demonstrate the efficacy of our approach by fabricating 3D serpentine flow channels 41 mm long in a volume of only  $0.12\ \text{mm}^3$ , and by printing high aspect ratio flow channels  $<25\ \mu\text{m}$  wide and 3 mm tall. These results indicate that 3D printing is finally positioned to challenge the pre-eminence of methods such as soft lithography for microfluidic device prototyping and fabrication.

### 1 Introduction

As evidenced by numerous recent reviews,<sup>1–10</sup> the advantages of 3D printing for microfluidic device fabrication are increasingly being recognized. Digital Light Processing stereolithography (DLP-SLA) is an especially attractive lower-cost 3D printing approach for microfluidics,<sup>11,12</sup> particularly since a microfluidic device is essentially a series of linked voids in a bulk material. During DLP-SLA fabrication, such voids are regions of unpolymerized resin that must be flushed after 3D printing, which is an easier process than trying to remove a solid sacrificial support as required by other 3D printer technologies such as polyjet.<sup>13,14</sup> Unfortunately, as we showed in Ref. 11, current commercial 3D printing tools and materials are unable to fabricate truly microfluidic voids ( $<100\ \mu\text{m}$ ), and hence 3D printed devices are at best in the large microfluidic regime ( $100\text{--}500\ \mu\text{m}$ ),<sup>14–20</sup> but more often in the millifluidic ( $>1\ \text{mm}$ )<sup>13,21–23</sup> or sub-millifluidic ( $0.5\text{--}1.0\ \text{mm}$ )<sup>24–30</sup> regimes (see Ref. 12 for a review of 3D printed

microfluidics in terms of these size categories).

We recently showed that custom resin formulation in conjunction with a relatively high resolution DLP-SLA 3D printer ( $27\ \mu\text{m}$  pixel pitch in the image plane) enabled us to 3D print microfluidic flow channels with cross sectional area ( $108\ \mu\text{m} \times 60\ \mu\text{m}$ ) near the boundary between the microfluidic and large microfluidic regimes.<sup>11</sup> We leveraged these advances to 3D print very compact valves and pumps, leading to the demonstration of high density integration of such components in a 3-to-2 microfluidic multiplexer with a fully 3D layout, thereby illustrating some of the advantages of 3D printing for microfluidics.<sup>31</sup>

In this paper, we show how 3D printing can be further extended to fabricate microfluidic flow channels with cross sectional area small enough to truly be in the microfluidic regime. Our approach is to construct our own high resolution 3D printer ( $7.6\ \mu\text{m}$  pixel pitch in the image plane) and develop a custom resin specifically tailored to take advantage of the 385 nm LED spectrum of the 3D printer. Moreover, we introduce a new channel narrowing technique that results in reliably printing flow channels as small as  $18 \times 20\ \mu\text{m}^2$ , which is 18 times smaller than our previous results in Ref. 11. To demonstrate the efficacy of our approach, we fabricate 41 mm long 3D serpentine flow channels in a volume of only  $1.56\ \text{mm} \times 0.38\ \text{mm} \times 0.21\ \text{mm} = 0.12\ \text{mm}^3$ . We also demon-

<sup>a</sup> Department of Electrical and Computer Engineering, Brigham Young University, Provo, UT 84602, United States; E-mail: nordin@byu.edu

<sup>b</sup> Department of Chemistry and Biochemistry, Brigham Young University, Provo, UT 84602, United States.

<sup>†</sup> Electronic Supplementary Information (ESI) available: [details of any supplementary information available should be included here]. See DOI: 10.1039/b000000x/

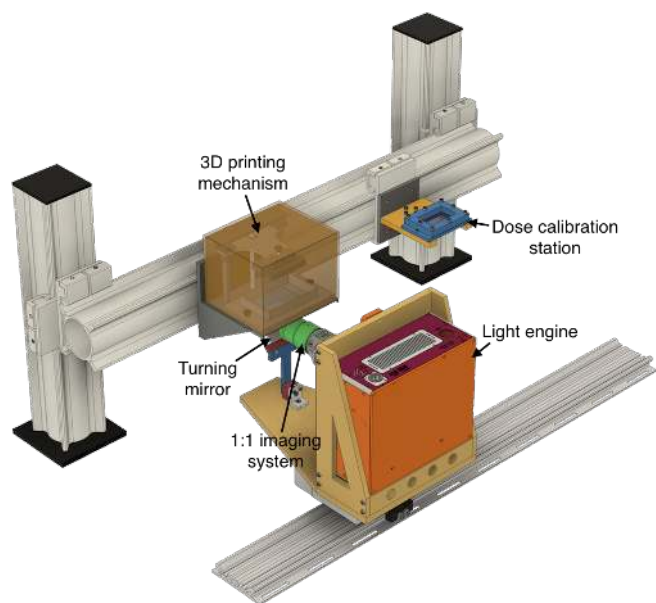


Fig. 1 3D CAD model of our custom 3D printer.

strate high aspect ratio channels  $<25\ \mu\text{m}$  wide and 3 mm tall. In short, we show that when appropriately applied, DLP-SLA is an effective method to 3D print truly microfluidic voids, which lays the foundation for 3D printing to challenge the dominance of conventional methods of microfluidic prototyping and development such as soft lithography and hot embossing.

## 2 Materials and methods

### 2.1 Custom 3D printer

Our two most important design criteria for constructing a custom 3D printer for microfluidics are a high resolution light engine and a UV LED light source. The former is critical to achieve small in-plane ( $x$ - $y$ ) void size, while the latter enables a wider selection of materials for custom resin formulation than the 405 nm sources we have previously worked with.<sup>11</sup> As we show in Sect. 3.1, creating a resin with the correct optical properties relative to the light source is critical to achieve small out-of-plane ( $z$  dimension) void size.

Our 3D printer design is shown in Fig. 1. A schematic illustration of its layout and operation is included in Fig. S1, ESI<sup>†</sup>. The 3D printer comprises a light engine, a  $45^\circ$  turning mirror with 3 axes of adjustment, a 3D printing mechanism, and custom-made mounts. The light engine and turning mirror are attached to a common base, which in turn is mounted to a rail so that the assembly can be conveniently shifted between the 3D printing mechanism on the left and a resin dose calibration set up (detailed in Sect. 2.4) on the right.

The light engine (Visitech, Lier, Norway) is based on a TI DLP9000 (Texas Instruments) containing a  $2560 \times 1600$  micromirror array. With a 1:1 imaging system, the image plane resolution is  $7.6\ \mu\text{m}$  and the projected area is  $19.35 \times 12.10\ \text{mm}^2$ . The optical source in the light engine is a 385 nm LED. We measure the peak wavelength and full-width at half-maximum (FWHM) of the source to be 383.4 nm and 12.6 nm, respec-

tively. The  $45^\circ$  turning mirror reflects light from the horizontally mounted light engine such that projected patterns can be focused through the transparent bottom of a resin tray. We heavily modified a Solus 3D printing mechanism (Junction3D, Santa Clarita, CA) to serve as a platform for the 3D printing process. The bottom of the resin tray is a replaceable teflon film that is tensioned on an underlying quartz window to guarantee flatness.

In its current configuration, the ultimate build size of our 3D printer is  $19.35\ \text{mm} \times 12.10\ \text{mm} \times 80\ \text{mm}$ , where the XY size and the Z size are determined by the projected image from the light engine and the Solus mechanism, respectively. Note that we have deliberately traded-off XY size in favor of higher XY resolution, which is required to obtain small in-plane void size. If desired, the XY build size can be increased without compromising resolution by exposing multiple images side-by-side for each layer. This can be accomplished, for example, by translating the light engine in XY. In this paper we use a single image position for each layer, and defer translating the light engine to future work.

We have developed custom Python software to operate our 3D printer. The software controls the 3D printing mechanism over a serial channel using G-code and the light engine over I<sup>2</sup>C to a low-level hardware interface. Images are sent with a graphics card through HDMI. All synchronization of 3D printer functions is performed in the Python code. The code gives us absolute control over all aspects of the 3D printer, including arbitrary exposure times for arbitrary layers during a 3D print, multiple independent exposures per layer, variable layer thicknesses, and, most importantly, single pixel precision in the projected images.

### 2.2 Materials

The focus of our resin formulation efforts is finding one or more UV absorbers that will give the optical properties needed to achieve small void size in the  $z$  dimension. Similar to our previous work,<sup>11,19,31</sup> we use poly(ethylene glycol) diacrylate (PEGDA, MW258) as the monomer and phenylbis(2,4,6-trimethylbenzoyl)phosphine oxide (Irgacure 819) as the photoinitiator. They are obtained from Sigma-Aldrich (St. Louis, MO) and BASF (Vandalia, Illinois), respectively.

Part of the motivation for use of a PEGDA-based resin is that we have already shown<sup>32</sup> that it has low non-specific adsorption and is suitable for electrophoretic separations. Moreover, Urrios et al. showed that their PEGDA resin formulation could be made biocompatible with a specific post-processing treatment.<sup>33</sup> Regarding solvent compatibility, we have found 3D printed PEGDA resins to be compatible with some solvents such as isopropyl alcohol and ethanol, but not others such as acetone and toluene.

As indicated in Fig. 2, we evaluate 20 potential UV absorbers. Their molecular structures are shown in Fig. S2, ESI<sup>†</sup>. Nearly all are inexpensive and readily available. The absorbers are avobenzene, 2,5-bis(5-tert-butyl-benzoxazol-2-yl)thiophene (Benetex OB+), disodium 4,4'-bis(2-sulfonatostyryl)biphenyl (Benetex OB-M1), benzenepropanoic acid (BLS 99-2), 2,3,6,7-tetrahydro-9-methyl-1H,5H-quinolizino(9,1-g)coumarin (Coumarin 102), Martius Yellow, morin hydrate, nitrofurazone, 2-nitrophenyl phenyl sulfide (NPS), 5,12-naphthacenequinone (NTAQ), oc-

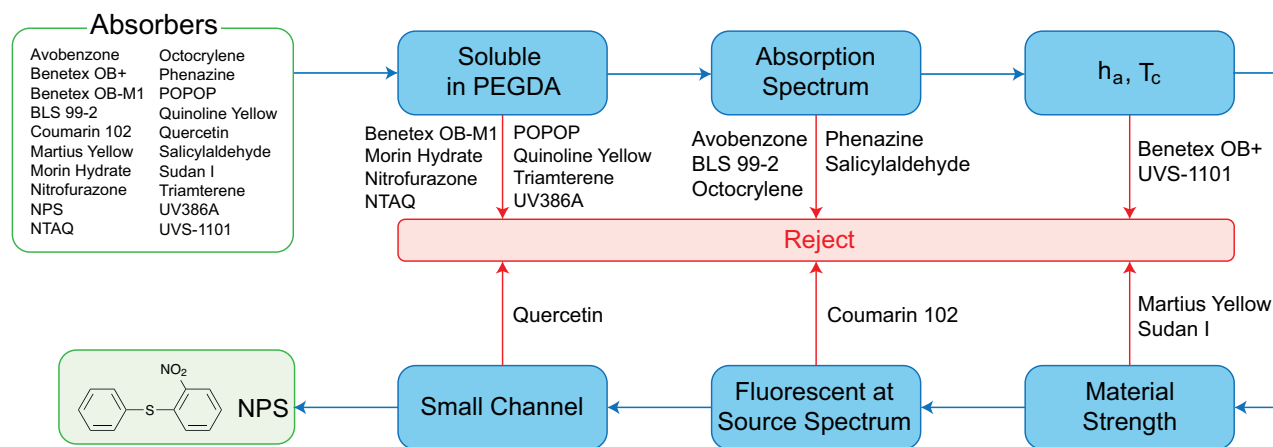


**Fig. 2** UV absorber evaluation criteria and process flow. 20 absorbers are initially considered. Rejected absorbers are indicated at each step in the process where they do not pass the evaluation criterion.

tocrylene, phenazine, 1,4-bis-(2-(5-phenyloxazolyl))-benzene (POPOP), Quinoline Yellow, 3,3',4',5,6-pentahydroxyflavone (Quercetin), salicylaldehyde, Sudan I, triamterene, UV386A, and 9,10-diethoxyanthracene (UVS-1101). Avobenzene and octocrylene are purchased from MakingCosmetics (Snoqualmie, WA); Benetex OB+, Martius Yellow, morin hydrate, Quinoline Yellow, quercetin, and Sudan I from Sigma-Aldrich (St. Louis, MO); Benetex OB-M1, nitrofurazone, and NPS from TCI America (Portland, OR); Coumarin 102, triamterene, and UVS-1101 from Alfa Aesar (Haverhill, MA); BLS 99-2 from Mayzo (Suwanee, GA); NTAQ and phenazine from Santa Cruz Biotechnology (Dallas, TX); salicylaldehyde from Thermo Fisher Scientific (Waltham, MA); and UV386A from QCR Solutions (St. Lucie, FL). Each chemical is used as received.

Resins studied for 3D printing are prepared by mixing 1% (w/w) Irgacure 819 and the desired concentration of UV absorber with PEGDA, and sonicating for 30 min. All photoinitiator-containing resins are stored in amber glass bottles after mixing.

### 2.3 Molar absorptivity measurement

The absorption spectrum of each UV absorber is measured by mixing the absorber at a specific concentration with PEGDA and placing a drop of resin in the gap between a glass slide and a coverslip separated by 65  $\mu\text{m}$  spacers. The resin is illuminated through the glass slide with attenuated light from a broadband XCITE-120Q source (Lumen Dynamics, Ontario, Canada). The transmitted light is captured by a fiber with 100  $\mu\text{m}$  diameter core connected to a QE65000 spectrometer (Ocean Optics, Dunedin, FL). The molar absorptivity is calculated from the measured absorption spectra of resins with and without an absorber, and from the known resin thickness.

### 2.4 Dose calibration

Polymerization thickness as a function of optical dose is measured with the set up on the right in Fig. 1, which consists of a custom resin container with a 75  $\times$  50  $\text{mm}^2$  glass window in the bottom. When the light engine is shifted on the rail to this calibration station, the height of the resin container is adjusted so that the pro-

jected image is focused on the top surface of the window. A layer of resin  $\sim$ 1 mm thick is applied to the window and exposed to a series of 1  $\text{mm}^2$  square patterns with different exposure times, which results in different polymerization depths. After rinsing unpolymerized resin with isopropyl alcohol (IPA), we measured the thickness of the polymerized regions using a Zeta-20 3D optical profilometer (Zeta Instruments, San Jose, CA).

### 2.5 3D printing

3D prints are fabricated on diced and silanized glass slides. The silanization procedure is given in Ref. 31, except that in the present work we use a silane concentration of 10% rather than 2%. All 3D prints are exposed with a measured optical irradiance of 21.2  $\text{mW}/\text{cm}^2$  in the image plane.

### 2.6 Material mechanical properties

As discussed in Sect. 3.2, we experimentally observe that some UV absorbers appear to hinder the photopolymerization process such that a given dose results in noticeably different material strengths for different absorbers. To illustrate this phenomenon, we measure the hardness and Young's modulus of two resins containing different UV absorbers. Measurements are made with 19.35  $\times$  12.10  $\times$  5  $\text{mm}^3$  3D printed blocks of polymerized resin printed with a 5  $\mu\text{m}$  layer thickness. Their Shore hardness is measured with a Rex Gauge Model 1600 durometer (Buffalo Grove, IL) for both ASTM D2240 Type A and Type D scales. The Young's Modulus is measured in compression with an Instron 3455 (Instron, Norwood, MA).

### 2.7 Post-print curing

In our previous paper,<sup>31</sup> 0.01% w/w azobisisobutyronitrile (AIBN) was added to the resin to enable post-print thermal curing to drive further polymerization and obtain improved mechanical properties. However, we find that the 385 nm source of our new 3D printer activates AIBN such that it is consumed during 3D printing, and is therefore unavailable for post-print thermal curing. We tried an alternate thermal initiator, benzoyl perox-

ide, but found that it was likewise activated during 3D printing. Therefore, we employ an optical curing approach in this paper. The key is to use a photoinitiator with absorbance that extends to longer wavelengths than the long wavelength cut off of the UV absorber such that light in this region penetrates through the device. For example, in Fig. 3(a), the Irgacure 819 absorption spectrum extends to  $\sim 460$  nm, while NPS and Martius Yellow drop off at  $\sim 440$  nm. For post-print optical curing we use an inexpensive consumer UV nail curer (54 Watt Professional UV Nail Dryer, Royal Nails) that emits a broad spectrum.

### 3 Results and discussion

In this section we begin by stepping through the process of developing a custom resin to fabricate truly microfluidic void sizes based on our new 3D printer, taking into account the source and UV absorber spectra. We develop a mathematical model from which the optical penetration depth for a resin,  $h_a$ , can be calculated directly from its measured molar absorptivity and desired absorber concentration, and also determine  $h_a$  and the critical exposure time,  $T_c$ , (see Ref. 11 for the model details) from experimental measurement of polymerization thickness as a function of exposure time. Our assessment leads to the selection of NPS as the UV absorber for our resins. Next, we evaluate the minimum achievable void size as a function of layer thickness and layer exposure time for 2% w/w NPS concentration. Using calculated dose as a function of  $z$ , we develop a model for the minimum achievable void size, and demonstrate that the model is predictive by applying it to 3% NPS resin to obtain flow channels with a design height of 18  $\mu\text{m}$ . We then introduce a new channel narrowing technique that reduces channel width from  $\sim 38$   $\mu\text{m}$  to  $\sim 20$   $\mu\text{m}$ . Finally, we demonstrate the utility of our methods by fabricating 41 mm long 3D serpentine flow channels and high aspect ratio flow channels.

#### 3.1 Absorber selection

##### 3.1.1 Criteria

Our approach to evaluating UV absorber candidates is illustrated in Fig. 2, which we apply to 20 candidate absorbers. These candidates were primarily found by examining chemical manufacturer websites and manually assessing absorption spectra in the 20 volumes of Ref. 34.

Most UV absorbers are powders that must be mixed with PEGDA, a liquid. The first test criterion is therefore whether the absorber is soluble. Table 1 shows the results of our solubility measurements. Seven of the 20 candidate absorbers are found to be insoluble in PEGDA and an eighth, nitrofurazone, has such a low solubility (0.07%) that it is unusable.

The next criterion is whether the absorber's absorption spectrum fully overlaps the emission spectrum of the light engine optical source. Fig. 3(a) shows the measured molar absorptivity as a function of wavelength for the remaining absorber candidates. It also shows the molar absorptivity of the photoinitiator, Irgacure 819, and the light engine source spectrum. As is evident from the figure, 5 absorber candidates have poor spectral overlap with the source. In each case, the absorber's long wavelength tail is insuf-

**Table 1** Solubility in PEGDA and fluorescence with 385 nm excitation. Dash indicates insolubility.

Material	Solubility (%)	Fluorescent
Avobenzone	>5	
Benetex OB+	0.25	Yes
Benetex OB-M1	—	Yes
BLS 99-2	>5	
Coumarin 102	0.8	Yes
Irgacure 819	>5	
Martius Yellow	3	
Morin Hydrate	—	
Nitrofurazone	0.07	
NPS	>5	
NTAQ	—	
Octocrylene	>5	
Phenazine	1.8	
POPOP	—	Yes
Quercetin	0.8	
Quinoline Yellow	—	
Salicylaldehyde	>5	
Sudan I	2.7	
Triamterene	—	Yes
UV386A	—	
UVS-1101	0.5	Yes

ficient to cover the full source spectrum. The result is that some of the source spectrum will penetrate deeper into the device during 3D printing, causing unpolymerized resin in what should be voids to polymerize and thereby fill the voids. Such absorbers are therefore incapable of being used to fabricate small voids, as we show below.

##### 3.1.2 Mathematical model

In Ref. 11 we noted that the polymerization depth,  $z_p$  for an exposure time of  $t_p$  is

$$z_p = h_a \ln \frac{t_p}{T_c}, \quad (1)$$

where  $h_a = 1/\alpha$  and  $\alpha$  is the resin's absorption coefficient. This result assumes monochromatic illumination, which is valid if the absorption coefficient is relatively constant over the source spectrum. However, in this paper we consider wavelength-dependent absorption such that we need to develop a more refined model.

Consider a photopolymerizable resin with absorption coefficient  $\alpha(\lambda)$  occupying the half space  $z \geq 0$  and illuminated by a polychromatic light source,  $I_0(\lambda)$ , from the  $-z$  direction. The dose ( $\text{J}/\text{cm}^2$ ) at  $z$  for exposure time  $t$  can be expressed as (see Sect. S3, ESI<sup>†</sup> for a comprehensive comparison of the monochromatic and polychromatic cases)

$$D(z, t) = t \int_0^\infty I_0(\lambda) e^{-\alpha(\lambda)z} d\lambda. \quad (2)$$

Normalizing by the dose at  $z = 0$  we obtain,

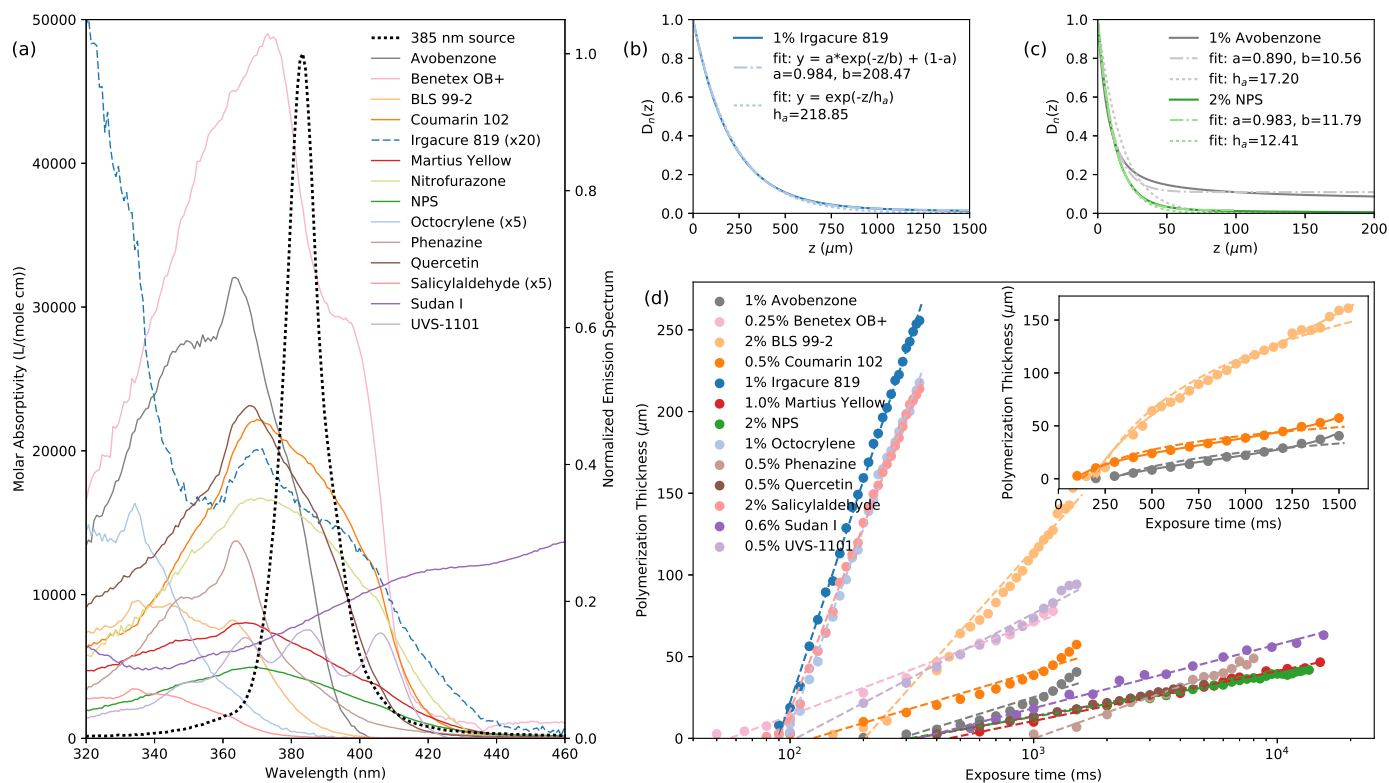


**Fig. 3** (a) Measured molar absorptivity and LED source spectrum. (b)  $D_n(z)$  calculated from molar absorptivity for 1% Irgacure 819 resin. (c) Same as (b) except for 1% Avobenzon and 2% NPS resins. (d) Measured polymerization thickness as a function of exposure time for 13 resins. Each resin contains 1% Irgacure 819 in addition to the specified UV absorber. Dashed lines indicate fit to Model 3. Inset shows that Model 4 (solid lines) is a better fit for some resins.

$$D_n(z) = \frac{D(z,t)}{D(0,t)} \quad (3)$$

$$= \frac{\int_0^\infty I_0(\lambda) e^{-\alpha(\lambda)z} d\lambda}{\int_0^\infty I_0(\lambda) d\lambda}. \quad (4)$$

The normalized dose,  $D_n(z)$ , indicates how rapidly the relative dose decreases as a function of  $z$ , and has the functional form of a weighted average of  $e^{-\alpha(\lambda)z}$  over  $\lambda$  with weighting function  $I_0(\lambda)$ . Based on many calculations with measured spectra for numerous absorbers, we have found that this weighted average can be approximated as

$$D_n(z) \approx ae^{-z/b} + c \quad (5)$$

$$= 1 - a(1 - e^{-z/b}), \quad (6)$$

where we have used  $c = 1 - a$  in Eq. 6, which can be derived from  $D_n(0) = 1$ . When there is good spectral overlap between an absorber and the source spectrum,  $a = 1$  and the approximation for  $D_n(z)$  reduces to

$$D_n(z) \approx e^{-z/h_a}, \quad (7)$$

where we have recognized that  $b = h_a$ . We refer to Eq. 7 as Model 1 and Eq. 6 as Model 2. Both depend solely on the spectral properties of the absorber and the source. Given the molar absorptivity,  $\epsilon(\lambda)$ , from Fig. 3(a), the absorption coefficient,  $\alpha(\lambda)$ , is

$$\alpha(\lambda) = \log(10)\epsilon(\lambda)C \quad (8)$$

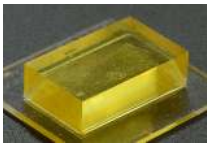
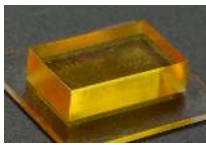
where the molar concentration,  $C$ , can be calculated from the w/w absorber concentration,  $C_{w/w}$ , in percent as

$$C = \frac{C_{w/w} \eta_P}{100 M_a} \quad (9)$$

in which  $\eta_P$  is the density of PEGDA and  $M_a$  is the absorber molar mass.

Figures 3(b) and (c) show example calculations of  $D_n(z)$  using Eqs. 4 and 8 for three resins based on their measured absorption spectra and the light engine source spectrum. As seen in Fig. 3(a), both Irgacure 819 and NPS have good spectral overlap with the source spectrum, such that fitting Model 2 to the calculated  $D_n(z)$  yields  $a$  very close to 1, in which case  $b$  from Model 2 and  $h_a$  from Model 1 agree to within 5%. On the other hand, avobenzon does not have good spectral overlap with the source such that  $a < 0.9$ , and  $b$  and  $h_a$  differ by 60%. Note that for Irgacure 819 and NPS,  $D_n(z) \rightarrow 0$  as  $z \rightarrow \infty$ , whereas for avobenzon

**Table 2** Comparison of Young's modulus and durometer measurements for NPS and Martius Yellow resins. Durometer measurements are unitless and Young's Modulus,  $E$ , is in MPa.

2% NPS				1.2% Martius Yellow			
							
$t_{exp}$ (ms)	A	D	E	$t_{exp}$ (ms)	A	D	E
280	86	21	3.5	500	84	—	2.7
400	94	52	6.6	1000	93	70	6.7
280 cured	97	75	7.7	500 cured	94	47	5.5

$D_n(z) \rightarrow \sim 0.1$ . Hence at depths beyond several  $h_a$ , NPS resin will remain largely unexposed, whereas avobenzene resin will continue to photopolymerize, making it unusable to fabricate small voids.

### 3.1.3 Polymerization as a function of dose

In Ref. 11 we utilized a resin characterization method in which the polymerization thickness is measured for a series of exposure times, followed by fitting the data to Eq. 1 to determine  $h_a$  and  $T_c$ . We employ a similar method in this paper, except that when there is poor spectral overlap between the absorber and the source spectrum, the polymerization behavior is better modeled by

$$t_p = \frac{T_c}{(1-a) + a \exp(-z_p/b)} \quad (10)$$

(see Sect. S4, ESI<sup>†</sup> for derivation). We refer to Eq. 1 as Model 3 and Eq. 10 as Model 4. These models' fit parameters are based solely on measured polymerization thickness as a function of optical exposure time.

Figure 3(d) shows the measured polymerization thickness as a function of exposure time for a wide selection of custom resins. In each case, the corresponding dashed line shows the fit to Model 3. The inset graph also shows the fit to Model 4 as solid lines for the three resins that have the poorest fit to Model 3 (1.0% avobenzene, 2% BLS 99-2, and 0.5% Coumarin 102).

The fits to Models 1 – 4 for all of the resins are shown in Table S2, ESI<sup>†</sup>. When the fit for  $a$  in Models 2 or 4 is  $\sim 1$ , the absorber has good spectral overlap with the source. In this case Models 1 and 3 are valid and typically show good agreement with each other even though they are generated from completely different measurements, thereby indicating the consistency of our analysis methods.

In addition to good spectral overlap, we also require that  $h_a$  be suitably small in order to realize 3D printed channels with small vertical void size. We therefore restrict our choice of absorbers to those that can achieve the smallest  $h_a$ , which, in conjunction with previous criteria, limits the possible absorbers to Coumarin 102, Martius Yellow, NPS, Quercetin, and Sudan I.

## 3.2 Material properties and layer dose

For a given irradiance and build layer thickness, the layer exposure time determines the dose and hence the degree of crosslinking in a layer. Smaller layer exposure times result in less crosslinking and hence less overall hardness and smaller Young's modulus. On the other hand, longer exposure time yields greater hardness and Young's modulus, but increases the exposure of resin in regions intended to be voids, thereby limiting the minimum vertical void size that can be achieved. There is thus a layer exposure time trade-off between material properties and minimum vertical void size. A resin that achieves adequate material properties with a smaller layer exposure time will yield a smaller vertical void size than a resin that requires a longer layer exposure time to obtain the same material properties.

As an example of the effect of two absorbers on material properties as a function of layer exposure time, consider 2% NPS and 1.2% Martius Yellow resins, which have  $h_a$  values of 11.2 and 9.8  $\mu\text{m}$ , respectively. Table 2 shows the results of Young's Modulus and Type A and D Shore durometer measurements. For 2% NPS, a layer exposure time of 280 ms yields a somewhat harder and stiffer material than a 500 ms layer exposure time for 1.2% Martius Yellow. When the materials undergo the same length post-print cure, the NPS resin still has greater hardness and Young's modulus. We therefore expect to achieve significantly smaller vertical void size with the NPS resin, which is consistent with our experimental observations.

In our experience making 3D printed valves and pumps,<sup>31</sup> post-print curing is necessary for long valve and pump operational lifetime. Since optical curing is necessary for the reasons discussed in Sect. 2.7, Sudan I is eliminated from consideration because its absorption spectrum extends far beyond the long wavelength limit of Irgacure 819 such that it cannot be optically cured to achieve good material properties.

## 3.3 Small cross section channels

Our ultimate criterion for absorber selection is which absorber(s) result in the smallest cross section channels. Experimentally we find that Coumarin 102 can yield small channels only when they are close to the last exposed layer; deeper channels are always closed. We ascribe this to the fact that Coumarin 102 is fluorescent at 385 nm. Since fluorescent light is emitted at longer wavelengths than the excitation light, and much of it is beyond the long wavelength cutoff of Coumarin 102 absorption, the fluorescent light can penetrate deeper during printing such that resin in underlying channels is exposed and polymerized. Resin in channels near the surface do not receive enough dose from fluorescence in subsequent layers to become polymerized.

In the case of Quercetin, we found that small channel sizes could be fabricated, but they exhibited internal delamination. While it may be possible to find conditions in which this does not occur, we chose to focus our efforts on the remaining absorber, NPS.

### 3.3.1 Channel height

Extensive testing with 2% NPS reveal a set of conditions that repeatedly result in the smallest possible channel height with essen-

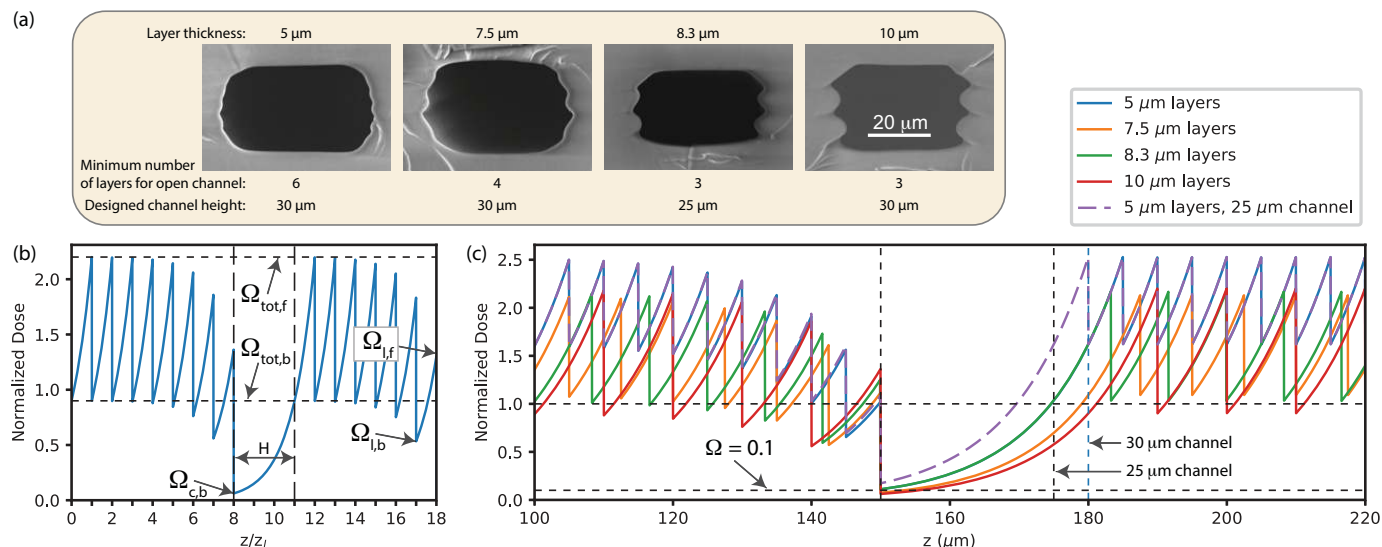


**Fig. 4** (a) SEM images of flow channel cross sections for 2% NPS. See text for details. All channels are designed to be 4 pixels wide. Larger layer thickness results in larger vertical wall surface relief. (b) Normalized dose as a function of normalized depth. (c) Calculated dose as a function of depth for the cases in (a).

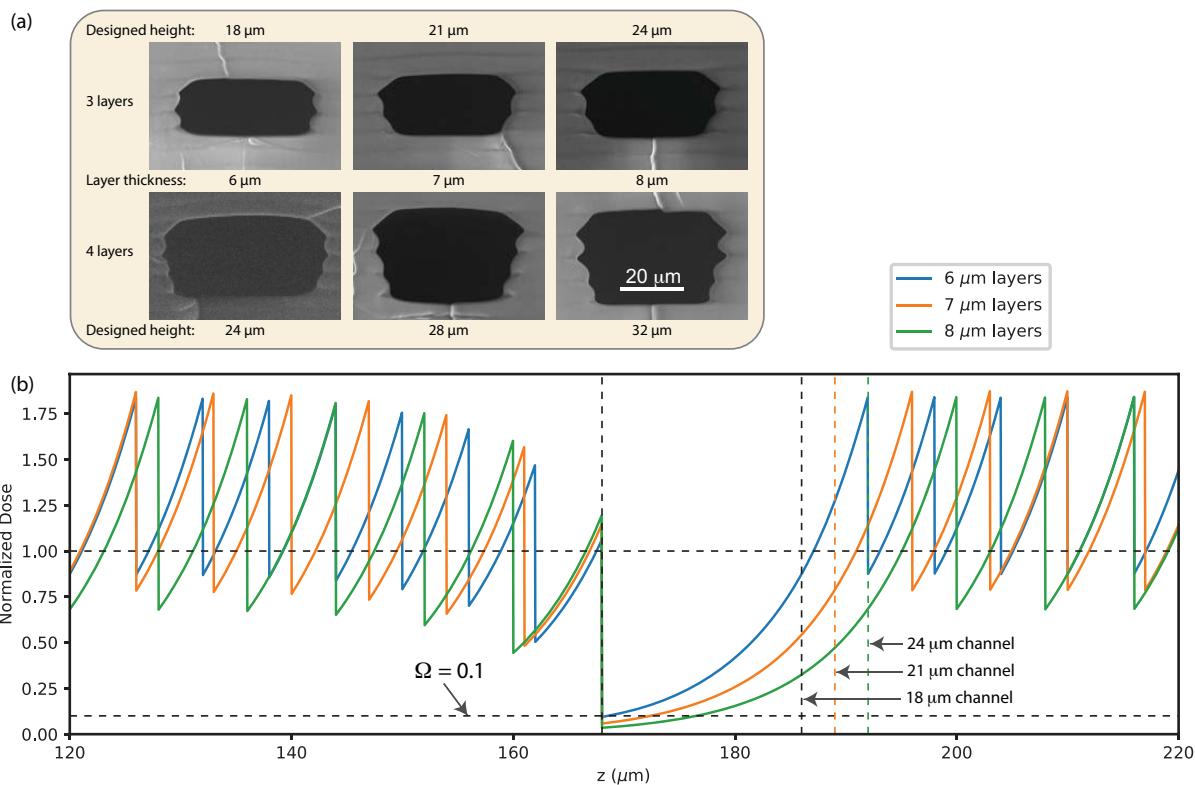


**Fig. 5** (a) Same as Fig. 4(a) except for 3% NPS. (b) Calculated normalized dose as a function of depth for the 3 layer cases in (a).

tially 100% yield. This can be illustrated with Fig. 4(a), in which scanning electron microscope (SEM) images of channel cross sections are shown for the smallest achievable channel height (30  $\mu\text{m}$ ) for layer thicknesses,  $z_l$ , of 5, 7.5, and 10  $\mu\text{m}$ . For 8.3  $\mu\text{m}$  layers, the smallest channel height is 25  $\mu\text{m}$ . A plot of normalized dose as defined in Ref. 11 ( $\Omega = D(z)/D_c$ ) is shown as a function of  $z/z_l$  for a generic case in Fig. 4(b) for the layers surrounding

a flow channel intended to occupy layers 8-10. The normalized dose at the top of the channel is  $\Omega_{\text{tot},b}$ , which exponentially decays through the thickness of the channel. Successful channel formation requires that this exponential tail is small enough to avoid significant polymerization of resin in the channel.

Fig. 4(c) shows the calculated normalized dose for the actual experimental conditions of Fig. 4(a). An additional example case



is shown for a 25  $\mu\text{m}$  channel made with 5  $\mu\text{m}$  layers, which never successfully forms clear channels. It is representative of many other parameter combinations that also fail. Experimentally, we find that the minimum height channel for a given layer thickness fulfills the following conditions: (1) the normalized dose at the back of the channel,  $\Omega_{c,b}$  is less than or equal to  $\sim 0.1$  and (2) the dose at the front of the channel,  $\Omega_{tot,b}$  is such that it decays to less than or equal to  $\sim 1$  at a distance of  $L_{min}$  above the bottom of the channel, where  $L_{min}$  is given by

$$L_{min} \approx -h_a \log(0.1) \quad (11)$$

$$= 2.3h_a. \quad (12)$$

Careful examination of the first 4 cases shown in Fig. 4(c) shows that these conditions are fulfilled ( $2.3h_a = 25\mu\text{m}$  for 2% NPS), whereas for the last case the second condition is not fulfilled ( $\Omega$  is  $\sim 1.7$  at  $25\mu\text{m}$ ).

The smallest possible channel height is realized when the designed channel is 3 layers thick with a height  $L_{min}$ , in which case the normalized layer thickness,  $\zeta_l$ , is

$$\zeta_l = z_l/h_a \quad (13)$$

$$\approx 0.77. \quad (14)$$

Channels larger than this are possible with other layer thicknesses as long as conditions (1) and (2) are fulfilled.

To test whether this model is predictive, consider 3% NPS resin for which  $h_a = 8\mu\text{m}$ , in which case

$$L_{min} = 2.3h_a = 18\mu\text{m} \quad (15)$$

$$z_l = L_{min}/3 = 6\mu\text{m} \quad (16)$$

$$\zeta_l = z_l/h_a = 0.75. \quad (17)$$

Figure 5(a) shows the corresponding results where the 3 layer 18  $\mu\text{m}$  channel is clearly open, as are 3 layer channels with 7 and 8  $\mu\text{m}$  layers. The calculated normalized dose as a function of  $z$  in Fig. 5(b) clearly fulfills the model's conditions for all cases. As seen in the second row of SEM images in Fig. 5(a), increasing the channel height by adding more layers always results in open channels.

### 3.3.2 Channel width

The designed channel width for all of the cases presented so far is 4 pixels (30  $\mu\text{m}$ ). Consistent with our results in Ref. 11, we found this to be the minimum channel width that gives 100% yield. However, the physical width of the channels in Figs. 4(a) and 5(a) are wider than the designed width by the equivalent of 1 to 2 pixels. This can be explained by noting that the teflon film at the bottom of the resin tray is slightly cloudy. It therefore causes scattering of the light imaged through it, which broadens the effective exposure region of each pixel that is turned on. Lack of

exposure for the pixels in the channel reduces the dose received at the edges of the channels to below the polymerization threshold.

We have developed a channel narrowing method that compensates for this lack of sufficient dose at channel edges. The left image in Fig. 6(a) shows a typical primary exposure pattern for a single layer containing a flow channel where white and black regions correspond to full exposure and no exposure, respectively. The right image is a second exposure of the same layer where only the 1 or 2 pixels adjacent to the channel are exposed. Figure 6(b) and (c) show the effect of 1 and 2 pixel edge exposures for different exposure times for 2% and 3% NPS resin, respectively. This strategy is clearly very effective in narrowing the channel width, which is further illustrated in Fig. 6(d) where the measured channel width is plotted as a function of the edge exposure time. The width can be reduced from nearly 40  $\mu\text{m}$  to 20  $\mu\text{m}$ . As shown in Fig. 6(e), the edge dose has no effect on the channel height (as expected). The final result is that 18  $\mu\text{m} \times 20\mu\text{m}$  channels can be consistently fabricated with 3% NPS resin.

### 3.4 Long channels

As an illustration of the efficacy of our approach, consider the fabrication of serpentine channels in Fig. 7 in 3% NPS resin with a 1 pixel 400 ms edge exposure. A microscope image of a single layer serpentine channel is shown in Fig. 7(a). Note the excellent optical clarity of imaging through the microscope slide substrate into the interior of the 3D printed device. A 3D serpentine channel design is shown in Fig. 7(b), with a photograph of a device containing 24 3D channels in Fig. 7(c). An SEM cross section is shown in Fig. 7(d). The channel is 41 mm long and occupies a volume of only 1.56 mm  $\times$  0.38 mm  $\times$  0.21 mm = 0.12 mm<sup>3</sup>.

### 3.5 Tall high aspect ratio channel

As a further demonstration, consider the high aspect ratio channel shown in Fig. 8, fabricated with 5  $\mu\text{m}$  layers, 4 pixels wide in 2% NPS with 2 pixel 400 ms edge exposure. Since we are not going for the minimum channel height, we can use a smaller layer thickness to decrease the sidewall surface relief that naturally occurs due to the layered nature of the 3D printing process. The channel width is  $< 25\mu\text{m}$  and its height is 3 mm (its length is 12 mm). Such channels are useful in nanoscale liposome synthesis for drug delivery as discussed in Ref. 35.

## 4 Conclusions

In summary, we have shown that DLP-SLA is fully capable of 3D printing truly microfluidic flow channels with designed cross sectional areas as small as 18  $\mu\text{m} \times 20\mu\text{m}$ . The out-of-plane void size is dependent on formulating a resin that adequately limits optical penetration during each layer exposure, which requires that the absorber's absorption spectrum fully cover the source spectrum. Small in-plane (x-y) void size is a function of the projected image resolution with a minimum width of 4 pixels. We have also shown that an additional edge dose for each layer containing a flow channel is an effective method of narrowing flow channel width. Taken together, these advances open the door for 3D

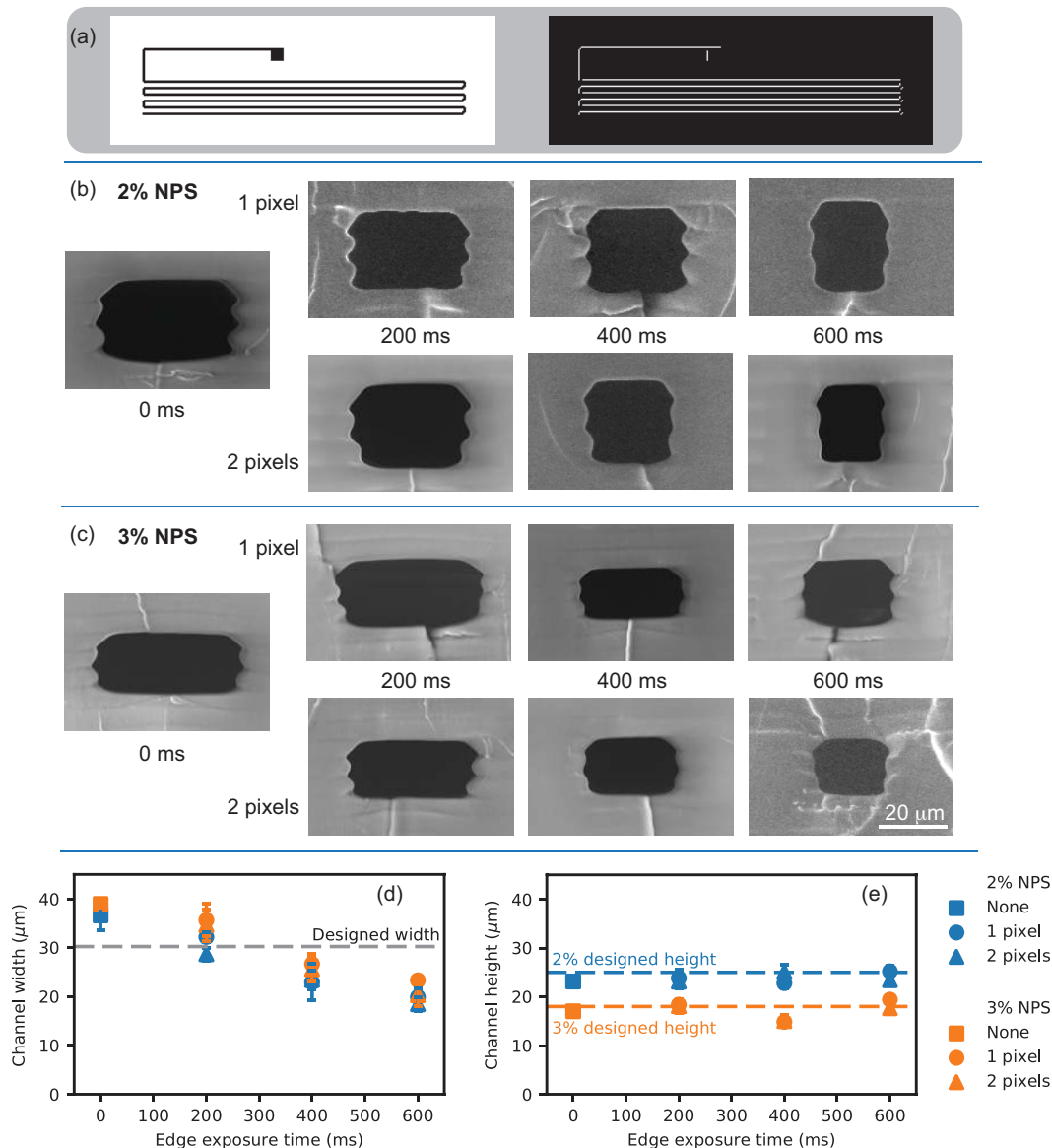


**Fig. 6** (a) Primary and additional edge exposure patterns for a single layer containing a flow channel. (b) Channel narrowing for 2% NPS resin for additional edge exposure. The build layer size is  $8.3 \mu\text{m}$  layers and the designed flow channel height is  $25 \mu\text{m}$ . (c) Same as (b) except for 3% NPS resin with  $6 \mu\text{m}$  layers and a designed flow channel height of  $18 \mu\text{m}$ . (d), (e) Measured channel width and height, respectively, as a function of edge exposure time.

printing to displace conventional microfluidic fabrication methods such as soft lithography.

## Conflicts of Interest

There are no conflicts of interest to declare.

## Acknowledgement

We are grateful to the National Institutes of Health (R01 EB006124) for partial support of this work. We also thank Dr. Radim Knob for taking many of the SEM images.

## References

- 1 A. K. Au, W. Huynh, L. F. Horowitz and A. Folch, *Angew. Chem.*, 2016, **128**, 3926–3946.
- 2 Y. He, Y. Wu, J.-z. Fu, Q. Gao and J.-j. Qiu, *Electroanalysis*, 2016, **28**, 1658–1678.
- 3 R. Amin, S. Knowlton, A. Hart, B. Yenilmez, F. Ghaderinezhad, S. Katebifar, M. Messina, A. Khademhosseini and S. Tasoglu, *Biofabrication*, 2016, **8**, 022001.
- 4 N. Bhattacharjee, A. Urrios, S. Kang and A. Folch, *Lab on a Chip*, 2016, **16**, 1720–1742.
- 5 S. Waheed, J. M. Cabot, N. P. Macdonald, T. Lewis, R. M. Guijt, B. Paull and M. C. Breadmore, *Lab on a Chip*, 2016, **16**, 1993–2013.
- 6 C. Chen, B. T. Mehl, A. S. Munshi, A. D. Townsend, D. M. Spence and R. S. Martin, *Analytical Methods*, 2016, **8**, 6005–6012.
- 7 A. A. Yazdi, A. Popma, W. Wong, T. Nguyen, Y. Pan and J. Xu,

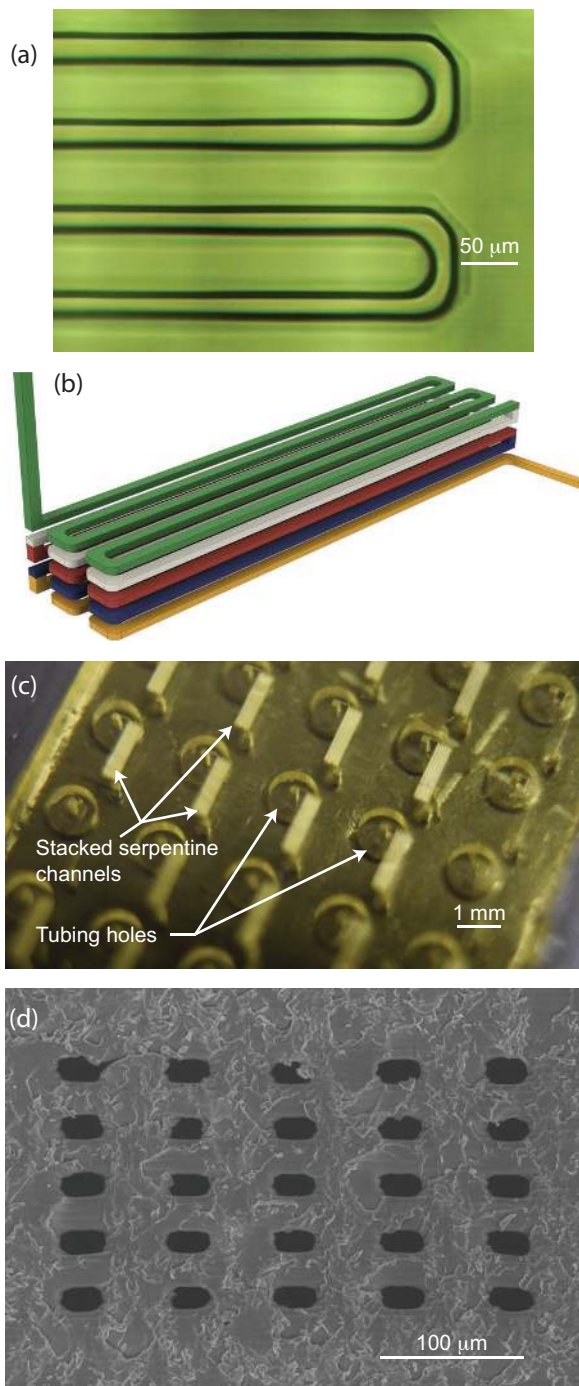


**Fig. 7** (a) Microscope photograph of single layer serpentine channel. (b) Schematic illustration of 3D stacked serpentine channel design. Each layer is shown as a different color. (c) Photograph of 3D printed device with 24 3D serpentine channels. The photo is taken through the glass slide on which the device is 3D printed. (d) SEM image of 3D serpentine channel cross section.

*Microfluidics and Nanofluidics*, 2016, **20**, 1–18.

- 8 C. M. B. Ho, S. H. Ng, K. H. H. Li and Y.-J. Yoon, *Lab Chip*, 2015, **15**, 3627–3637.
- 9 Y. Huang, M. C. Leu, J. Mazumder and A. Donmez, *Journal of Manufacturing Science and Engineering*, 2015, **137**, 014001.
- 10 B. C. Gross, J. L. Erkal, S. Y. Lockwood, C. Chen and D. M.

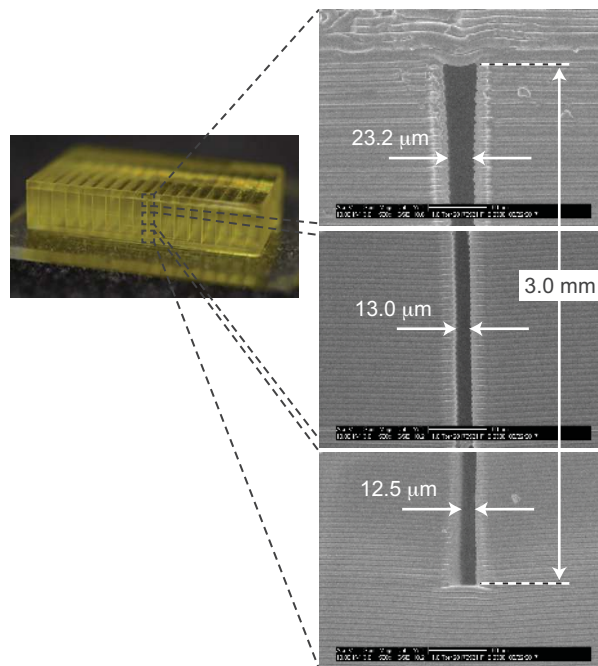


**Fig. 8** Photograph and SEM images of 3D printed high aspect ratio flow channel.

Spence, *Anal. Chem.*, 2014, **86**, 3240–3253.

- 11 H. Gong, M. Beauchamp, S. Perry, A. T. Woolley and G. P. Nordin, *RSC Adv.*, 2015, **5**, 106621–106632.
- 12 M. J. Beauchamp, G. P. Nordin and A. T. Woolley, *Analytical and Bioanalytical Chemistry*, 2017, 1–9.
- 13 R. D. Sochol, E. Sweet, C. C. Glick, S. Venkatesh, A. Avetisyan, K. F. Ekman, A. Raulinaitis, A. Tsai, A. Wienkers, K. Korner, K. Hanson, A. Long, B. J. Hightower, G. Slatton, D. C. Burnett, T. L. Massey, K. Iwai, L. P. Lee, K. S. J. Pister and L. Lin, *Lab Chip*, 2016, **16**, 668–678.
- 14 R. Walczak and K. Adamski, *Journal of Micromechanics and Microengineering*, 2015, **25**, 085013.
- 15 Y. Ukita, Y. Takamura and Y. Utsumi, *Japanese Journal of Applied Physics*, 2016, **55**, 06GN02.
- 16 A. I. Shallan, P. Smejkal, M. Corban, R. M. Guijt and M. C. Breadmore, *Anal. Chem.*, 2014, **86**, 3124–3130.
- 17 J. M. Lee, M. Zhang and W. Y. Yeong, *Microfluidics and Nanofluidics*, 2016, **20**, 5.
- 18 L. Donvito, L. Galluccio, A. Lombardo, G. Morabito, A. Nicolosi and M. Reno, *Journal of Micromechanics and Microengineering*, 2015, **25**, 035013.
- 19 C. I. Rogers, K. Qaderi, A. T. Woolley and G. P. Nordin, *Biomicrofluidics*, 2015, **9**, 1–9.
- 20 N. P. Macdonald, J. M. Cabot, P. Smejkal, R. M. Guijt, B. Paull and M. C. Breadmore, *Analytical Chemistry*, 2017, **89**, 3858–3866.
- 21 K. G. Lee, K. J. Park, S. Seok, S. Shin, J. Y. Park, Y. S. Heo, S. J. Lee, T. J. Lee et al., *RSC Advances*, 2014, **4**, 32876–32880.
- 22 K. B. Anderson, S. Y. Lockwood, R. S. Martin and D. M. Spence, *Analytical chemistry*, 2013, **85**, 5622–5626.

- 23 P. S. Venkateswaran, A. Sharma, S. Dubey, A. Agarwal and S. Goel, IEEE Sensors Journal, 2016, **16**, 3000–3007.
- 24 H. N. Chan, Y. Shu, B. Xiong, Y. Chen, Y. Chen, Q. Tian, S. A. Michael, B. Shen and H. Wu, ACS Sensors, 2015, **1**, 227–234.
- 25 A. Urrios, C. Parra-Cabrera, N. Bhattacharjee, A. M. Gonzalez-Suarez, L. G. Rigat-Brugarolas, U. Nallapatti, J. Samitier, C. A. DeForest, F. Posas, J. L. Garcia-Cordero et al., Lab on a Chip, 2016, **16**, 2287–2294.
- 26 G. W. Bishop, J. E. Satterwhite-Warden, I. Bist, E. Chen and J. F. Rusling, ACS sensors, 2015, **1**, 197–202.
- 27 K. C. Bhargava, B. Thompson and N. Malmstadt, Proceedings of the National Academy of Sciences, 2014, **111**, 15013–15018.
- 28 W. G. Patrick, A. A. Nielsen, S. J. Keating, T. J. Levy, C.-W. Wang, J. J. Rivera, O. Mondragón-Palomino, P. A. Carr, C. A. Voigt, N. Oxman et al., PloS one, 2015, **10**, e0143636.
- 29 J. M. Zhang, E. Q. Li, A. A. Aguirre-Pablo and S. T. Thoroddsen, RSC Advances, 2016, **6**, 2793–2799.
- 30 A. J. Morgan, L. H. San Jose, W. D. Jamieson, J. M. Wymant, B. Song, P. Stephens, D. A. Barrow and O. K. Castell, PloS one, 2016, **11**, e0152023.
- 31 H. Gong, A. T. Woolley and G. P. Nordin, Lab on a Chip, 2016, **16**, 2450–2458.
- 32 C. I. Rogers, J. V. Pagaduan, G. P. Nordin and A. T. Woolley, Anal. Chem., 2011, **83**, 6418–6425.
- 33 A. Urrios, C. Parra-Cabrera, N. Bhattacharjee, A. M. Gonzalez-Suarez, L. G. Rigat-Brugarolas, U. Nallapatti, J. Samitier, C. A. DeForest, F. Posas, J. L. Garcia-Cordero and A. Folch, Lab on a Chip, 2016, 1–8.
- 34 L. Láng, Absorption Spectra in the Ultraviolet and Visible Region, Academic Press, 1961.
- 35 R. R. Hood and D. L. DeVoe, small, 2015, **11**, 5790–5799.

# Electronic Supporting Information

## Custom 3d printer and resins for $18 \mu\text{m} \times 20 \mu\text{m}$ microfluidic flow channels

### S1 3D Printer

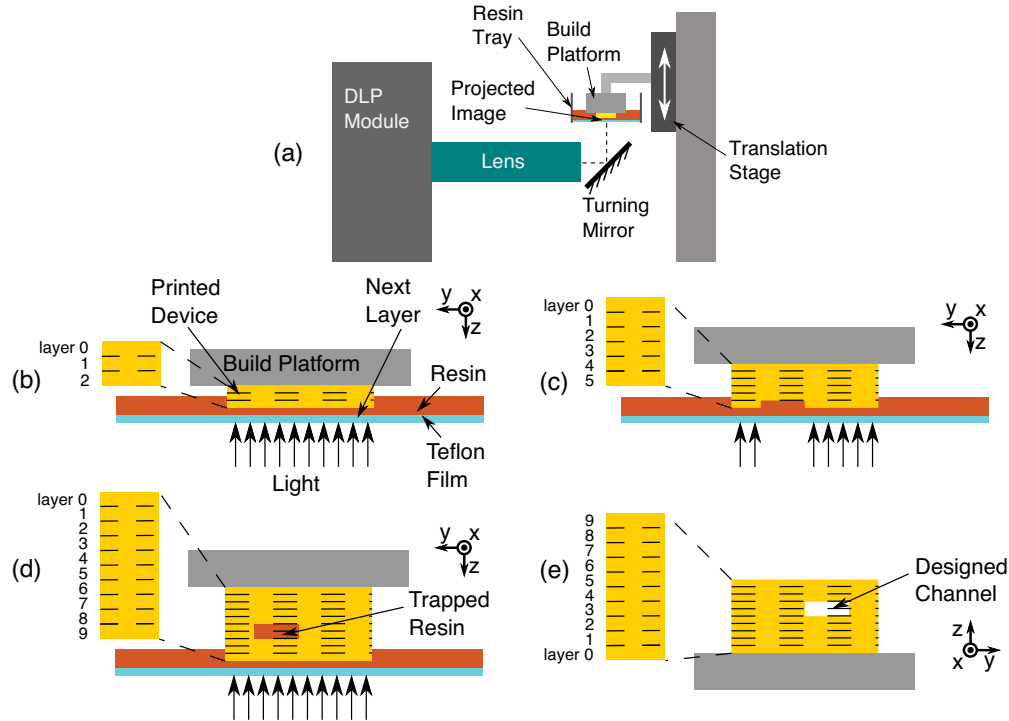


Figure S1: (a) Schematic illustration of 3D printer. (b)-(e) Process to 3D print a device, illustrating the formation of a microfluidic flow channel (i.e., void region).

Fig. S1(a) shows a schematic illustration of our 3D printer and the spatial relationship between the various components. During operation (Fig. S1(b)-(e)), a device is fabricated upside down with light incident through a transparent Teflon film which comprises the bottom of the resin tray. Each layer is formed by raising the build platform several millimeters to permit fresh resin to flow into the space between the Teflon film and the last built layer, followed by lowering the build platform such that the last built layer is separated from the Teflon film by  $z_l$ , the build layer thickness. The uncured resin in this space is then photopolymerized in the desired pattern by exposure to an image projected by the DLP module, lens system, and turning mirror.

We have done some preliminary characterization using SEM measurements for 2% NPS resin of the actual build layer thicknesses achieved by our system compared to the design thicknesses of 5, 7.5, 8.3, and  $10 \mu\text{m}$ . This analysis shows that the average measured build layer thickness is 7.6% smaller than the designed thickness with a standard deviation of 7.5%. A few initial measurements for the 3% NPS resin design thicknesses of 6 and  $7 \mu\text{m}$  show measured thicknesses that are 12% smaller. While better build layer thickness fidelity can likely be achieved by replacing the stock Solus z-translation mechanism with one having higher performance, we have found the stock mechanism to be sufficient for the purposes of this paper in which we demonstrate how to achieve  $18 \mu\text{m} \times 20 \mu\text{m}$  3D printed flow channels.

## S2 Molecular structures

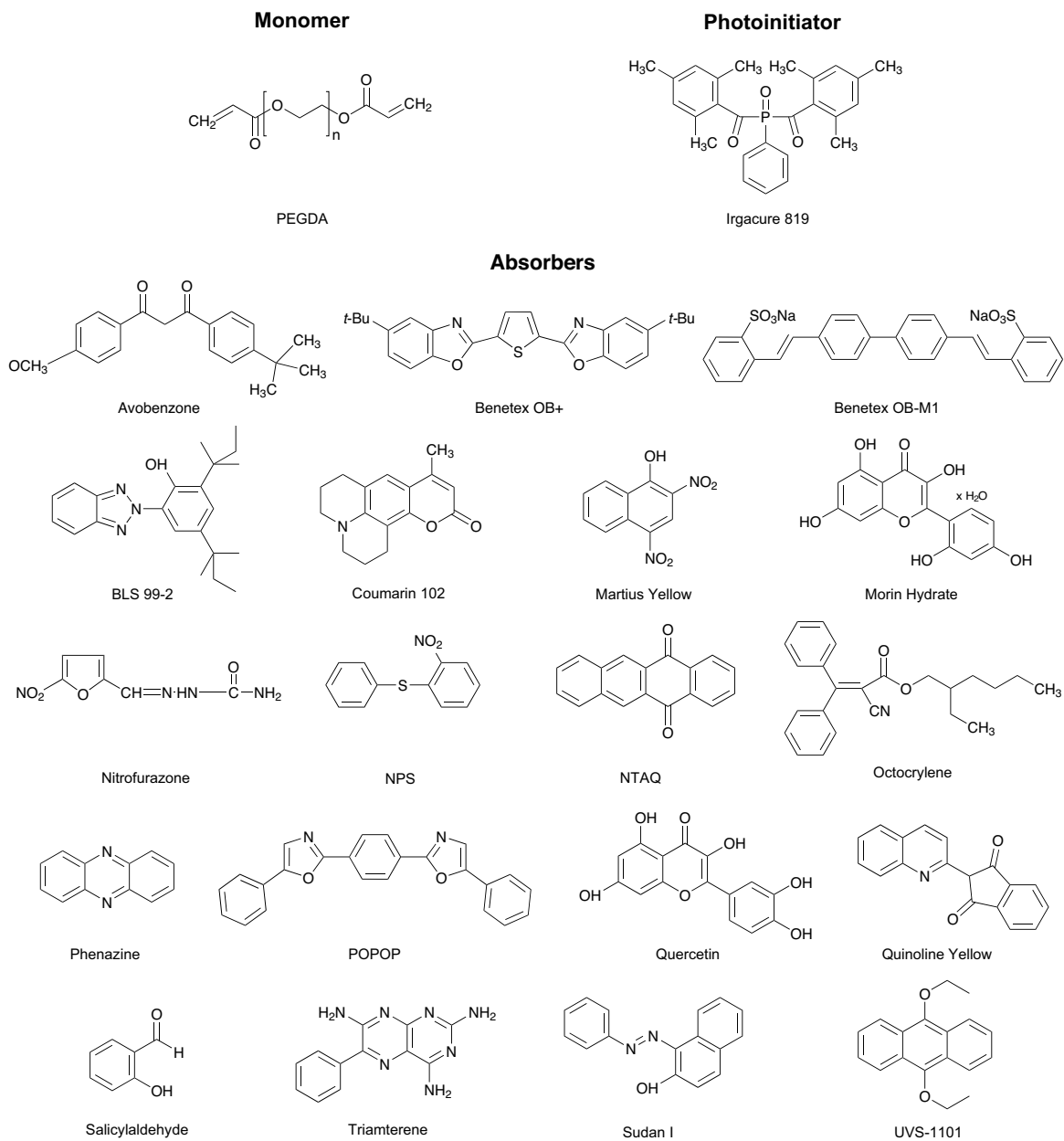


Figure S2: Molecular structures for monomer, photoinitiator, and UV absorbers used in this study (except for UV386A, which is proprietary).

Table S1: Comparison of monochromatic and polychromatic resin exposures

Line	Parameter	Units	Symbol	Monochromatic Case	Polychromatic Case
1	Irradiance at $z = 0$	W/cm <sup>2</sup>	$I_0$	$I_0$	$\int_0^\infty I_0(\lambda) d\lambda$
2	Irradiance as a function of $z$	W/cm <sup>2</sup>	$I(z)$	$I_0 e^{-\alpha z}$	$\int_0^\infty I_0(\lambda) e^{-\alpha(\lambda)z} d\lambda$
3	Dose as a function of $z, t$	J/cm <sup>2</sup>	$D(z, t)$	$t I_0 e^{-\alpha z}$	$t \int_0^\infty I_0(\lambda) e^{-\alpha(\lambda)z} d\lambda$
4	Critical dose	J/cm <sup>2</sup>	$D_c$	$t_p I_0 e^{-z_p/h_a}$	$t_p \int_0^\infty I_0(\lambda) e^{-\alpha(\lambda)z_p} d\lambda$
5	Time to reach critical dose at $z = 0$	s	$T_c$	$D_c/I_0$	$D_c/\int_0^\infty I_0(\lambda) d\lambda$
6	Polymerization depth	$\mu\text{m}$	$z_p$	$h_a \ln \frac{t_p}{T_c}$	see below

### S3 Monochromatic and polychromatic resin exposure comparison

Table S1 summarizes the parameters that are important for monochromatic exposure of photopolymerizable resins as defined in Ref. 1. It also gives the corresponding expressions for polychromatic resin exposures so the two cases can be directly compared.

### S4 Derivation of Model 4

The critical dose,  $D_c$ , on Line 4 in Table S1 is the dose required to just polymerize a resin for a given irradiance. This dose occurs at the leading edge of the polymerization thickness,  $z_p$ , which corresponds to a specific polymerization time,  $t_p$ . *For the monochromatic case* we can solve Line 4 for the polymerization time (using Line 5) as

$$\frac{t_p}{T_c} = e^{z_p/h_a}, \quad (\text{S1})$$

which leads to Eq. 1 for  $z_p$  in the main text (Model 3, which is also on Line 6).

*For the polychromatic case* we cannot obtain an analytic expression for the polymerization depth,  $z_p$ . Instead, we must solve for  $t_p$ . Beginning with Line 5,

$$T_c = \frac{D_c}{\int_0^\infty I_0(\lambda) d\lambda}, \quad (\text{S2})$$

and substituting for  $D_c$  (Line 4), we obtain

$$\frac{T_c}{t_p} = \frac{\int_0^\infty I_0(\lambda) e^{-\alpha(\lambda)z_p} d\lambda}{\int_0^\infty I_0(\lambda) d\lambda} \quad (\text{S3})$$

$$= D_n(z_p) \quad (\text{S4})$$

$$\approx (1 - a) + a \exp(-z_p/b) \quad (\text{S5})$$

where  $D_n(z)$  is the normalized dose defined in Eq. 3 and Eq. S5 is from Eq. 6 in the main text. Solving for  $t_p$  we obtain

$$t_p = \frac{T_c}{(1 - a) + a \exp(-z_p/b)}, \quad (\text{S6})$$

which is Model 4.

Table S2: Summary of fit parameters based on measured spectra and on measured thickness vs. exposure time data. All resins are formulated with 1% Irgacure 819 in addition to the specified absorber.

Material	Solubility	Concentration	Fit from measured spectrum			Fit from measured thickness vs. exposure time				
			Model 1	Model 2		Model 3		Model 4		
			$h_a$ ( $\mu\text{m}$ )	$a$	$b$ ( $\mu\text{m}$ )	$h_a$ ( $\mu\text{m}$ )	$T_c$ (ms)	$a$	$b$ ( $\mu\text{m}$ )	$T_c$ (ms)
<b>Photoinitiator</b>										
Irgacure 819	>5%	1%	218.85	0.98	208.47	196.13	89.42	1.00	193.40	88.21
<b>UV Absorbers</b>										
Avobenzon	>5%	1%	15.10	0.92	10.70	20.00	283.23	0.84	10.49	258.93
Benetex OB+	0.25%	0.25%	19.15	0.97	17.50	24.47	56.37	0.98	21.65	55.95
BLS 99-2	>5%	2%	57.28	0.97	50.65	72.49	202.13	0.92	51.30	181.92
Coumarin 102	0.8%	0.5%	11.98	0.97	11.03	19.55	123.59	0.95	12.00	90.90
Martius Yellow	3%	1%	15.26	0.98	14.34	13.28	448.69	1.00	13.03	423.74
NPS	>5%	2%	11.74	0.98	11.17	11.18	307.33	1.00	10.88	280.44
NPS		3%	8.28	0.99	7.94	8.05	413.72	1.00	8.16	427.58
Octocrylene	>5%	1%	194.96	0.98	184.13	173.84	95.75	1.00	173.00	95.27
Phenazine	1.8%	0.5%	33.47	0.97	30.30	23.03	1005.38	0.96	19.51	936.94
Quercetin	0.8%	0.5%	16.16	0.96	14.12	12.03	324.96	1.00	12.18	333.04
Salicylaldehyde	>5%	2%	175.21	0.98	166.75	162.94	90.05	1.00	164.19	90.58
Sudan I	2.7%	0.6%	18.08	1.00	17.99	16.92	335.62	1.00	14.95	227.14
UVS-1101	0.5%	0.5%	31.20	0.98	28.92	34.03	105.75	0.96	24.11	78.80

## S5 Fits to Models 1–4

As seen in Table S2, absorbers with good spectral overlap with the source spectrum as observed in Fig. 3(a) have fits to Model 2 in which  $a \approx 1$ . In this case Model 2 reduces to Model 1 and the corresponding fits for  $b$  and  $h_a$  are in reasonable agreement. Likewise, when Models 3 and 4 are fit to experimental thickness versus exposure data, good spectral overlap corresponds to  $a = 1$  in Model 4 such that Model 4 reduces to Model 3 and  $b$  and  $h_a$  are fairly consistent with not only each other, but also with  $b$  and  $h_a$  obtained solely from the measured molar absorptivity in Models 1 and 2. An important ramification is that for absorbers with good spectral overlap with the source it is unnecessary to experimentally measure the thickness as a function of exposure to determine  $h_a$ . Instead,  $h_a$  can be found by using it as a fitting parameter in Eq. 7 in the main text where the absorption coefficient in  $D_n(z)$  is

$$\alpha(z) = \alpha_{abs}(\lambda) + \alpha_{pi}(\lambda) \quad (\text{S7})$$

where  $\alpha_{abs}(\lambda)$  and  $\alpha_{pi}(\lambda)$  are the absorber and photoinitiator absorption coefficients, respectively, calculated from their molar absorptivities.

## References

- [1] H. Gong, M. Beauchamp, S. Perry, A. T. Woolley and G. P. Nordin, *RSC Adv.*, 2015, **5**, 106621–106632.